DOI: 10.1002/chem.200800013

Hypervalent versus Nonhypervalent Carbon in Noble-Gas Complexes

Simon C. A. H. Pierrefixe,[a] Jordi Poater,[a] Chan Im,[b] and F. Matthias Bickelhaupt*[a]

Abstract: Silicon in $[Cl{-}SiH_3{-}Cl]^-$ is hypervalent, whereas carbon in $[Cl{-}CH_3{-}Cl]^-$ is not. We have recently shown how this can be understood in terms of the ball-in-a-box model, according to which silicon fits perfectly into the box that is constituted by the five substituents, whereas carbon is too small and, in a sense, "drops to the bottom" of the box. But how does carbon acquire hypervalency in the isostructural and isoelectronic noble gas (Ng)/methyl cation complexes $[Ng{-}CH_3{-}Ng]^+$ (Ng = He and Ne), which feature a delocalized D_{3h}-symmetric structure with two equivalent C–Ng bonds? From Ng = Ar onwards, the $[Ng{-}CH_3{-}Ng]^+$ complex again acquires a propensity to localize one of its axial C–Ng bonds and to largely break the other one, and this propensity increases in the order Ng = Ar < Kr < Xe < Rn. The behavior of the helium and neon complexes violates the ball-in-a-box principle. Why does this happen? The purpose of this study is to answer these questions and to understand why carbon can become truly hypervalent under certain conditions. To this end, we have carefully analyzed the structure and bonding in $NgCH_3Ng^+$ and, for comparison, CH_3Ng^+, $NgHNg^+$, and NgH^+. It appears that, at variance with $[Cl{-}CH_3{-}Cl]^-$, the carbon atom in $[Ng{-}CH_3{-}Ng]^+$ can no longer be considered as a ball in a box of the five substituents.

Keywords: bond theory · carbon · density functional calculations · hypervalent compounds · noble gases

Introduction

It is well-known that silicon in $[Cl{-}SiH_3{-}Cl]^-$ is hypervalent, whereas carbon in $[Cl{-}CH_3{-}Cl]^-$ is not.[1–3] Recently, we explained this difference in valency in terms of the ball-in-a-box model.[1] In this model, the five substituents form a ClH_3Cl^- cage or "box" in which they are in mutual steric contact. The central atom can be viewed as a "ball" in that box. Silicon fits perfectly into the box that is constituted by the five substituents to give a hypervalent configuration with delocalized, equivalent Si–Cl bonds (**I**). The carbon atom, on the other hand, is too small and, in a sense, "drops to the bottom" of the box, and this leads to a species $Cl^-\cdots H_3CCl$ (**II**) with one localized C–Cl bond, one long C···Cl contact, and a pyramidalized CH_3 unit. Our findings for $ClCH_3Cl^-$ and $ClSiH_3Cl^-$ have been generalized to other Group 14 central atoms (Ge, Sn, and Pb) and another axial substituent (F).[1]

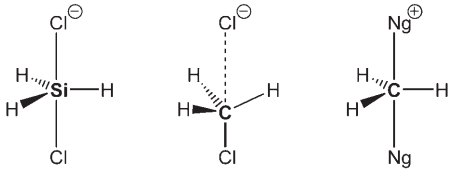

I II III

But why then does carbon become a hypervalent atom in the isostructural and isoelectronic noble gas/methyl cation complexes $[Ng{-}CH_3{-}Ng]^+$ (Ng = He and Ne),[4] which feature delocalized D_{3h}-symmetric structure with two equivalent C–Ng bonds (**III**)?[4a] For Ng = Ar, the $[Ng{-}CH_3{-}Ng]^+$ complex again acquires a propensity to localize one of its axial C–Ng bonds and to largely break the other.[4a] Why is that so? And does this propensity for localization persist or, possibly, further increase along the series Ng = Ar, Kr, Xe, and Rn?

[a] Dr. S. C. A. H. Pierrefixe, Dr. J. Poater, Dr. F. M. Bickelhaupt
Department of Theoretical Chemistry
and Amsterdam Center for Multiscale Modeling
Scheikundig Laboratorium der Vrije Universiteit
De Boelelaan 1083, 1081 HV Amsterdam (The Netherlands)
Fax: (+31) 20-598-7629
E-mail: FM.Bickelhaupt@few.vu.nl

[b] Dr. C. Im
Department of Chemistry, Konkuk University
1 Hwayang-dong, Gwangjin-gu, Seoul, 143-701 (Korea)

Supporting information for this article is available on the WWW under http://www.chemeurj.org/ or from the author.

The purpose of this study is to answer the above questions and to understand why carbon can become truly hypervalent under certain conditions. To this end, we carefully analyzed the structure and bonding in $NgCH_3Ng^+$ and, for comparison, CH_3Ng^+, $NgHNg^+$, and NgH^+ by DFT with relativistic corrections for species involving Kr, Xe, and Rn, as implemented in the ADF program.[5,6] The bonding analyses consist of decomposition of the total bond energy into interaction energies between fragments of the overall model systems, that is, methyl cation + noble gas. The trends in the various energy terms are interpreted in the conceptual framework provided by the quantitative molecular orbital (MO) model contained in Kohn–Sham DFT.[7] We compare the results of the present analyses of noble-gas complexes $NgCH_3Ng^+$ with those previously obtained for the halogen-substituted XCH_3X^- and $XSiH_3X^-$ species.[1]

In addition, to validate our DFT approach, we first computed accurate ab initio benchmarks for the helium, neon, and argon complexes using a hierarchical series of ab initio methods up to CCSD(T).[8] The ab initio calculations were carried out with the Gaussian program suite[9] and they support our DFT approach.

Interestingly, it appears that, at variance with the situation of $[Cl{-}CH_3{-}Cl]^-$, the carbon atom in $[Ng{-}CH_3{-}Ng]^+$ can no longer be considered as a ball in a box of the five substituents. Instead, the $[Ng{-}CH_3{-}Ng]^+$ species are better conceived as a "disk between balls". Here, the "disk" is CH_3^+ and the "balls" are the two noble-gas atoms. We propose a spectrum of five-coordinate carbon species that ranges from the ball-in-a-box situation to the disk-between-balls model, depending on the ratio of bond strengths between axial and equatorial substituents on carbon.

Methods Section

DFT calculations: DFT calculations were performed for all species using the Amsterdam Density Functional (ADF) program developed by Baerends and others[5] with the OLYP and BP86 functionals[6] in combination with the TZ2P basis set, which is a large uncontracted set of Slater-type orbitals (STOs) containing diffuse functions. This basis set of triple-ζ quality for all atoms was augmented with two sets of polarization functions, that is, 2p and 3d on H and He, 3d and 4f on C, Ne, and Ar, 4d and 4f on Kr, 5d and 4f on Xe, and 6d and 5f on Rn. The core shells of carbon and neon (1s), argon (1s2s2p), krypton (1s2s2p3s3p), xenon (1s2s2p3s3p4s3d4p), and radon (1s2s2p3s3p4s3d4p5s4d5p) were treated by the frozen-core approximation. An auxiliary set of s, p, d, f, and g STOs was used to fit the molecular density and to represent the Coulomb and exchange potentials accurately in each self-consistent field cycle. Relativistic effects were taken into account in calculations of species involving Kr, Xe, or Rn atoms using the zeroth-order regular approximation (ZORA).[5c] All stationary points were confirmed to be equilibrium structures (no imaginary frequency) or transition states (one imaginary frequency) through vibrational analysis.

Ab initio calculations: Ab initio calculations were carried out for $NgCH_3Ng^+$ and CH_3Ng^+ (Ng = He, Ne, Ar) with the Gaussian program suite[9] with a hierarchical series of methods: Møller–Plesset perturbation theory[8a] of second order (MP2) and fourth order (MP4) and coupled-cluster theory[8b] with single and double excitations as well as triple excitations treated perturbatively [CCSD(T)].[8c] These calculations were done with the Pople 6-311++G** basis set[10] at each level of theory and the Dunning correlation-consistent polarized valence basis set of triple-ζ quality (cc-pVTZ)[11] at the MP2 and MP4 levels. The geometries for the $ArCH_3Ar^+$ systems were, due to the enormous computational demand, all optimized at the MP2/6-311++G** level. Energies at a higher level of theory for these species were computed in a single-point fashion using the MP2/6-311++G** geometries. This approach was verified for the CH_3Ar^+ system to yield deviations in relative energies of only a few hundredths of a kilocalorie per mole.

Bond analyses: To gain more insight into the nature of the bonding in our noble gas/methyl cation complexes, an energy decomposition analysis was carried out.[7] In this analysis, the total binding energy ΔE associated with forming the overall molecular species of interest, say AB, from two fragments A′ + B′ is made up of two major components [Eq. (1)].

$$\Delta E = \Delta E_{\text{prep}} + \Delta E_{\text{int}} \tag{1}$$

In this formula, the preparation energy ΔE_{prep} is the amount of energy required to deform the individual (isolated) fragments from their equilibrium structure (A′, B′) to the geometry that they acquire in the overall molecule (A, B). The interaction energy ΔE_{int} corresponds to the actual energy change when these geometrically deformed fragments A and B are combined to form the molecular species AB. It is analyzed in the framework of the Kohn–Sham molecular orbital (MO) model by using a quantitative decomposition of the bond into electrostatic interaction, Pauli repulsion (or exchange repulsion or overlap repulsion), and (attractive) orbital interactions [Eq. (2)].[7]

$$\Delta E_{\text{int}} = \Delta V_{\text{elstat}} + \Delta E_{\text{Pauli}} + \Delta E_{\text{oi}} \tag{2}$$

The term ΔV_{elstat} corresponds to the classical electrostatic interaction between the unperturbed charge distributions $\rho_A(r)+\rho_B(r)$ of the deformed fragments A and B (vide infra for definition of the fragments) that adopt their positions in the overall molecule AB, and is usually attractive. The Pauli repulsion term ΔE_{Pauli} comprises the destabilizing interactions between occupied orbitals and is responsible for the steric repulsion. This repulsion is caused by the fact that two electrons with the same spin can not occupy the same region in space (cf. Pauli principle). It arises as the energy change associated with the transition from the superposition of the unperturbed electron densities $\rho_A(r)+\rho_B(r)$ of the geometrically deformed but isolated fragments A and B to the wavefunction $\Psi^0 = N\hat{A}[\Psi_A\Psi_B]$, which properly obeys the Pauli principle through explicit antisymmetrization ($\hat{A}$ operator) and renormalization (N constant) of the product of fragment wavefunctions (see ref. [7a] for an exhaustive discussion). The orbital interaction ΔE_{oi} in any MO model, and therefore also in Kohn–Sham theory, accounts for charge transfer (i.e., donor–acceptor interactions between occupied orbitals on one moiety with unoccupied

Abstract in Korean:

[Cl-SiH$_3$-Cl]$^-$내의 규소는 초과원자가이나 [Cl-CH$_3$-Cl]$^-$내의 탄소는 그렇지 않다. 우리는 최근에 이것을 어떻게 이해할 수 있는지에 대해서 규소는 다섯 개의 치환기로 구성된 상자에 완벽하게 맞는 반면 탄소는 상자의 바닥으로 떨어진다고 할 수 있을 만큼 너무 적기 때문이라는 상자 안의 공 모델의 관점을 이용하여 보였다. 그러나 어떻게 탄소가 두 개의 동등한 C-Ng 결합으로 비편재화된 D_{3h} 대칭구조를 특징으로 하는 동일구조 및 동일전자적 성질의 영족기체 메틸 양이온 복합체 [Ng-CH$_3$-Ng]$^+$내에서 초과원자가 성질을 갖게 되는가? 그것은 Ng 가 He 와 Ne 일 때이다. Ng 가 아르곤(Ar)인 경우부터, [Ng-CH$_3$-Ng]$^+$복합체는 다시 하나의 축선상 C-Ng 결합에 편재되고 다른 하나는 멀리 떨어지려는 경향을 갖게 되며 이러한 경향은 Ng = Ar, Kr, Xe 과 Rn 의 순서로 증가한다. 이러한 헬륨과 네온 복합체의 현상은 상자 안의 공 원리에 반한다! 왜 이런 현상이 일어나는가? 본 연구의 목적은 이러한 질문들에 답하고 왜 탄소가 이러한 상황에서 진성 초과원자가가 되는지를 이해하는 것이다. 마지막에 우리는 $NgCH_3Ng^+$와 비교를 위한 CH_3Ng^+, $NgHNg^+$와 NgH^+내에서의 구조와 결합을 면밀히 분석하였다. [Cl-CH$_3$-Cl]$^-$에 반하여 [Ng-CH$_3$-Ng]$^+$내의 탄소원자는 더 이상 다섯 개의 치환기를 갖는 상자 안의 공으로 취급될 수 없는 것이 명백하게 되었다.

orbitals of the other, including the HOMO–LUMO interactions) and polarization (empty–occupied orbital mixing on one fragment due to the presence of another fragment).[7] Since the Kohn–Sham MO method of DFT in principle yields exact energies and, in practice, with the available density functionals for exchange and correlation, rather accurate energies, we have the special situation that a seemingly one-particle model (an MO method) in principle completely accounts for the bonding energy.[7a] In particular, the orbital-interaction term of Kohn–Sham theory comprises the often distinguished attractive contributions charge transfer, induction (polarization), and dispersion. One could in the Kohn–Sham MO method try to separate polarization and charge transfer, as has been done by Morokuma[12] in the Hartree–Fock model, but this distinction is not sharp. In fact, contributions such as induction and charge transfer, and also dispersion, can be given an intuitive meaning, but whether, and with what precision, they can be quantified remains a controversial subject. In view of the conceptual difficulties, we refrain from further decomposing the KS orbital interaction term, except by symmetry (see below).

The orbital interaction energy can be further decomposed into contributions from each irreducible representation Γ of the interacting system [Eq. (3)] using the extended transition state (ETS) scheme developed by Ziegler and Rauk[7c–e] (note again that our approach differs in this respect from the Morokuma scheme,[12] which instead attempts a decomposition of the orbital interactions into polarization and charge transfer).

$$\Delta E_{oi} = \sum_{\Gamma} \Delta E_{\Gamma} = \Delta E_{\sigma} + \Delta E_{\pi} \quad (3)$$

In our model systems, the irreducible representations can be categorized into A and E symmetries, which correspond to what are commonly designated σ- and π-electron systems, respectively. This gives rise to the orbital-interaction components ΔE_{σ} and ΔE_{π}, as shown in Equation (3).

Atomic charges were computed by using the Voronoi deformation density (VDD) method[13] and the Hirshfeld scheme.[14]

Table 1. Geometric parameters r [Å] and θ [°] and complexation energies ΔE [kcal mol^{-1}] of C_{3v}-symmetric CH_3Ng^+ complexes (Ng = He, Ne, Ar).[a]

	CH_3He^+ C_{3v}			CH_3Ne^+ C_{3v}			CH_3Ar^+ C_{3v}		
	r	θ	ΔE	r	θ	ΔE	r	θ	ΔE
OLYP/A	1.701	92.8	−1.74	2.170	91.6	−2.89	2.012	99.0	−20.61
CCSD(T)/B	1.882	91.0	−1.86	2.168	91.1	−3.45	1.985	99.1	−17.94
experiment	2.176[b]			2.300[b]		−1.8 ± 0.3[c]	2.053[b]		−21.8 ± 2.0[c]

[a] Basis sets A, and B correspond to TZ2P and 6-311++G** (see also Methods Section). [b] IRPD data from reference [4a]. [c] Based on high-pressure MS enthalpies of −1.2 ± 0.3 and −19.8 ± 2.0 kcal mol^{-1} from reference [4i] with internal 298.15 K energy and $\Delta(pV)$ corrections of +0.57 and 2.04 kcal mol^{-1} for CH_3Ne^+ and CH_3Ar^+, respectively, from OLYP/TZ2P frequency calculations.

Table 2. Geometric parameters r, r_1, r_2 [Å] and θ [°] and Ng + CH_3Ng^+ complexation energies ΔE [kcal mol^{-1}] of D_{3h}- and C_{3v}-symmetric $NgCH_3Ng^+$ complexes (Ng = He, Ne, Ar).[a]

	$HeCH_3He^+$ D_{3h}		$NeCH_3Ne^+$ D_{3h}		$ArCH_3Ar^+$ C_{3v}				$ArCH_3Ar^+$ D_{3h}	
	r	ΔE	r	ΔE	r_1	r_2	θ	ΔE	r	ΔE
OLYP/A	2.123	−0.62	2.395	−1.76	2.030	3.528	98.6	−1.30	2.429	−0.48
CCSD(T)/B	2.047	−1.38	2.261	−2.92	1.991[b]	2.941[b]	98.7[b]	−2.91[b]	2.385[b]	−2.08[b]
experimental			2.344[c]					−2.5 ± 0.2[d]		

[a] r, r_1, r_2 are C–Ng distances; θ is the H-C-Ng angle. Basis sets A and B correspond to TZ2P and 6-311++G** (see also Methods Section). [b] Single-point energy calculation at MP2/6-311++G** geometry. [c] IRPD data from reference [4a]. [d] Based on high-pressure MS enthalpy of (−2.26 ± 0.20) kcal mol^{-1} from reference [4b] with internal 298.15 K energy and $\Delta(pV)$ correction of +0.26 kcal mol^{-1} from OLYP/TZ2P frequency calculation.

Results and Discussion

Ab initio benchmarks and DFT validation

Geometries: First, we computed ab initio benchmark geometries and C–Ng complexation energies of CH_3Ng^+ and $NgCH_3Ng^+$ for Ng = He, Ne, and Ar against which we can assess the performance of our DFT approach. The benchmarks derive from a hierarchical series of ab initio methods: MP2, MP4, and CCSD(T) which were evaluated in combination with the basis sets 6-311++G** (basis B) and, in the case of MP2 and MP4, cc-pVTZ (basis C). Our highest-level ab initio and DFT results are summarized in Tables 1 and 2, together with the scarcely available C–Ng bond lengths from infrared photodissociation (IRPD) experiments and complexation energies from high-pressure mass spectrometry. Full data of our benchmark and validation study can be found in Tables S1 and S2 in the Supporting Information, and definitions of geometric parameters in Scheme 1.

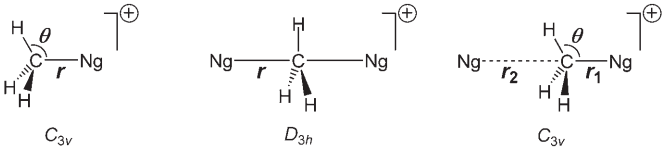

Scheme 1. Definition of geometric parameters in our model systems.

It is clear from Tables 1 and 2 and from Tables S1 and S2 in the Supporting Information that C–Ng distances (r, r_1, r_2) and H-C-Ng angles (θ) are converged along the hierarchical series of ab initio methods within a few hundredths of an angstrom and a few tenths of a degree, respectively. We recall, however, that the geometries of the C_{3v}- and D_{3h}-symmetric $ArCH_3Ng^+$ species were evaluated in all cases only at the MP2/B level because of the large computational costs for these systems. The CCSD(T)/B values for C–Ng distances in CH_3Ng^+ are 1.882 (He), 2.168 (Ne), and 1.985 Å (Ar) and those in the equilibrium structures of $NgCH_3Ng^+$ are 2.047 (He, D_{3h}), 2.261 (Ne, D_{3h}) and 1.991 Å (Ar, r_1, C_{3v}; from MP2/B). These ab initio geometries agree well with previous computations by Dopfer and others.[4] The discrepancy with the IRPD experimental C–Ng distances, which are about 0.1–0.3 Å longer than those obtained at CCSD(T) (and also at MP2 and MP4), has previously been ascribed to

the strong angular-radial coupling effect on the vibrationally averaged experimental C–Ng distances.[4e]

The OLYP/TZ2P values for C–Ng distances and H-C-Ng angles θ agree within about a tenth of an angstrom and about one degree (see Tables 1 and 2). Deviations are somewhat larger for the BP86 data, but this DFT approach still reproduces the ab initio benchmark trends (see Tables S1 and S2 in the Supporting Information). There is one noticeably larger deviation, namely, the long C–Ng distance r_2 in C_{3v}-symmetric Ng···CH_3Ng^+: the OLYP value here is about 0.5 Å longer than the MP2 value. While OLYP indeed somewhat underestimates the corresponding bond energy (vide infra), this deviation in r_2 is also to a large extent ascribed to the extreme shallowness of the associated potential energy well. This softness in the potential means that small changes in the level of theory and thus small changes in the bond energy may still lead to relatively large fluctuations in r_2.

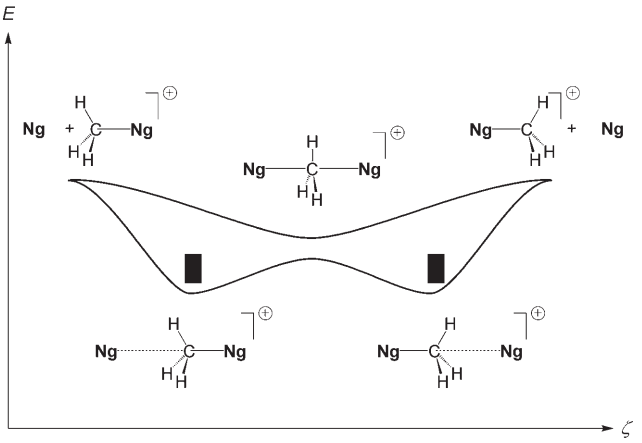

Figure 1. Single-well (top line: Ng = He, Ne) and double-well (bottom line: Ng = Ar–Rn) potential energy surface along the S_N2 reaction coordinate ζ of Ng + CH_3Ng^+.

Energies: Next, we examine the potential energy surfaces of the above species. Here, the OLYP approach turns out to excel more pronouncedly as compared to BP86 than in the case of the geometries. But first we consider the ab initio benchmark study. It is again clear from Tables S1 and S2 in the Supporting Information that the energies ΔE of CH_3Ng^+ [defined by reaction (4)] and of $NgCH_3Ng^+$ [defined by reaction (5)] are converged along the hierarchical series of ab initio methods within a few tenths of a kilocalorie per mole.

$$CH_3^+ + Ng \rightarrow CH_3Ng^+ \quad (4)$$

$$Ng + CH_3Ng^+ \rightarrow NgCH_3Ng^+ \quad (5)$$

The CCSD(T)/B values for ΔE of CH_3Ng^+ are −1.86 (He), −3.45 (Ne), and −17.94 kcal mol^{-1} (Ar), and those in the equilibrium structures of $NgCH_3Ng^+$ are −1.38 (He, D_{3h}), −2.92 (Ne, D_{3h}), and −2.91 kcal mol^{-1} (Ar, C_{3v}). Note that, in the case of Ng = Ar, the equilibrium structure is a C_{3v}-symmetrical reactant complex Ar···CH_3Ar^+ and that the D_{3h}-symmetric $[Ar{-}CH_3{-}Ar]^+$ is a transition state at ΔE = −2.08 kcal mol^{-1}, that is, +0.83 kcal mol^{-1} above the unsymmetrical reactant complex (compare top and bottom PES in Figure 1). These ab initio relative energies again agree well with the available results from previous studies.[4] High-pressure mass spectrometric complexation enthalpies ΔH for reaction (4) of CH_3Ne^+ and CH_3Ar^+ are (−1.2 ± 0.3) and (−19.8 ± 2.0) kcal mol^{-1}, and that for reaction (5) of $ArCH_3Ar^+$ is (−2.26 ± 0.20) kcal mol^{-1}.[4b,i] For a more consistent comparison with our theoretical data, we have converted these experimental enthalpies into energies using 298 K internal energies and $\Delta(pV)$ corrections based on OLYP/TZ2P frequency calculations. This yields an estimate of the experimental complexation energies ΔE of (−1.8 ± 0.3) and (−21.8 ± 2.0) kcal mol^{-1} for reaction (4) of CH_3Ne^+ and CH_3Ar^+ (see Table 1) and (−2.5 ± 0.2) kcal mol^{-1} for reaction (5) of $ArCH_3Ar^+$ (see Table 2).

The OLYP/TZ2P approach, as pointed out above, agrees well with the ab initio benchmark and experimental data: relative energies typically agree within about 1 kcal mol^{-1} with a somewhat larger deviation of about 2.5 kcal mol^{-1} in the case of CH_3Ar^+. Importantly, the trends in relative energies are correctly reproduced by OLYP: 1) a slight increase in ΔE from CH_3He^+ to CH_3Ne^+ and a significant stabilization from CH_3Ne^+ to CH_3Ar^+; and 2) a slight strengthening in ΔE from $HeCH_3He^+$ to $NeCH_3Ne^+$, a very subtle weakening from $NeCH_3Ne^+$ to Ar···CH_3Ar^+ and, notably, the occurrence, in the latter, of a weakly labile D_{3h}-symmetric $[Ar{-}CH_3{-}Ar]^+$ species that lies 0.82 kcal mol^{-1} above two C_{3v}-symmetric reactant complexes which it separates along an S_N2 reaction pathway (compare top and bottom PES in Figure 1). The BP86/TZ2P approach fails in particular regarding the qualitative trend of having stable D_{3h}-symmetric, pentavalent $[He{-}CH_3{-}He]^+$ and $[Ne{-}CH_3{-}Ne]^+$ complexes but a labile five-coordinate $[Ar{-}CH_3{-}Ar]^+$ that localizes one of the C–Ar bonds and partially breaks the other to give the asymmetric Ar···CH_3Ar^+ equilibrium structure (see Table S2 in the Supporting Information).

In conclusion, OLYP/TZ2P agrees well with the ab initio benchmarks for Ng = He, Ne, and Ar and performs better than the BP86/TZ2P approach. Therefore, in the following, we carried out our computations and analyses for the full range of systems, that is, for Ng = He, Ne, Ar, Kr, Xe, and Rn, using OLYP/TZ2P in combination with ZORA relativistic effects for Kr, Xe, and Rn.

Structure and bonding in $[CH_3{-}Ng]^+$: The C–Ng bond strength ΔE of the CH_3Ng^+ complexes increases monotonically on descending Group 18: from −1.7 (He) to −2.9 (Ne) to −20.6 (Ar) to −30.2 (Kr) to −42.6 (Xe) to −49.3 kcal mol^{-1} (Rn), as computed at the (ZORA-)OLYP/TZ2P level (see Table 3). Thus, the previously obtained trend of a systematic C–Ng bond strengthening along Ng = He, Ne, and Ar continues also for the heavier noble gases, down to radon.

Table 3. Analysis of the C–Ng bond between CH_3^+ and Ng in CH_3Ng^+ (Ng = He, Ne, Ar, Kr, Xe, and Rn).[a]

	CH_3He^+	CH_3Ne^+	CH_3Ar^+	CH_3Kr^+	CH_3Xe^+	CH_3Rn^+
	geometric parameters [Å, °]					
r(C–Ng)	1.701	2.170	2.012	2.114	2.242	2.320
θ(H-C-Ng)	92.8	91.6	99.0	100.1	101.8	102.3
C–H	1.094	1.094	1.089	1.089	1.088	1.088
	bond-energy decomposition [kcal mol^{-1}][b]					
ΔE_{oi}	−16.47	−9.94	−71.58	−88.46	−111.62	−120.21
ΔE_{Pauli}	17.51	8.65	57.12	63.84	73.16	72.95
ΔV_{elstat}	−3.36	−1.79	−12.26	−13.25	−14.64	−13.45
ΔE_{int}	−2.32	−3.08	−26.71	−37.87	−53.10	−60.72
ΔE_{prep}	0.58	0.19	6.10	7.72	10.54	11.38
$\Delta E(CH_3^+ + Ng)$	−1.74	−2.89	−20.61	−30.15	−42.56	−49.34
$\Delta E(Ng + CH_3Ng^+)$[c]	(−0.62)	(−1.76)	(−1.30)	(−1.65)	(−1.99)	(−2.21)
	$\langle Ng \mid CH_3^+ \rangle$ fragment orbital overlap					
$\langle$HOMO$\mid$LUMO$\rangle$	0.27	0.13	0.27	0.29	0.31	0.30
	fragment orbital energy [eV]					
Ng: HOMO a_1	−15.783	−13.604	−10.209	−9.163	−8.141	−7.556
	fragment orbital population [e]					
Ng: HOMO a_1	1.90	1.93	1.60	1.55	1.42	1.32
CH_3^+: LUMO a_1	0.11	0.07	0.39	0.45	0.58	0.65
noble-gas atomic charge [a.u.]						
Q^{VDD}	0.26	0.18	0.42	0.48	0.54	0.58
$Q^{Hirshfeld}$	0.18	0.16	0.47	0.54	0.63	0.68

[a] Computed at the OLYP/TZ2P level with ZORA relativistic effects for Ng = Kr, Xe, and Rn. See also Methods Section. [b] $\Delta E = \Delta E_{prep} + \Delta E_{int} = \Delta E_{prep} + \Delta V_{elstat} + \Delta E_{Pauli} + \Delta E_{oi}$. See also Methods Section. [c] For comparison: ΔE associated with adding a second Ng to CH_3Ng^+ with formation of the $NgCH_3Ng^+$ equilibrium structure (D_{3h} for Ng = He, Ne; C_{3v} for Ng = Ar, Kr, Xe, Rn).

Our analyses show that this trend derives mainly from the systematic increase in the energy of the valence 1s or *n*p atomic orbitals (AOs) along the series of noble-gas atoms, from −15.8 eV for He 1s to −7.6 eV for Rn 6p (see Table 3). The dominant feature in the bonding mechanism is the HOMO–LUMO interaction between the occupied noble-gas valence AO and the methyl cation $2a_1$ LUMO in the σ-electron system (see Figure 2a). Note that the σ-orbital interactions provide about 90% or more of the total orbital interactions ΔE_{oi} in all model systems analyzed and thus determine the trend in this term (not shown in the tables). In the beginning of our series, for Ng = He and Ne, the HOMO–LUMO gap is large and ΔE_{oi} as well as variations therein are small. Due to a decrease in the bond overlap as we go from He 1s to Ne 2p, the net result in ΔE_{oi} is a slight weakening. But overall the result is a (very) small increase in C–Ng bond strength ΔE from −1.7 to −2.9 kcal mol^{-1} (see Table 3).

The trend becomes more pronounced along Ne, Ar, Kr, Xe, and Rn. Now both the HOMO–LUMO gap (which decreases) and the bond overlap (which increases towards a plateau) work in concert and cause the orbital interactions ΔE_{oi} and thus the net C–Ng bond strength ΔE to increase markedly, as mentioned above [see Table 3 and Eq. (2)]. Note in particular the sharp increase in C–Ng bond strength from −2.9 to −20.6 kcal mol^{-1} as one goes from CH_3Ne^+ to CH_3Ar^+.

The overall trend in bond strengths ΔE and especially that in ΔE_{oi} is nicely reflected by the trend in the gross population P of the CH_3^+ $2a_1$ LUMO in CH_3Ng^+ (P = 0.11, 0.07, 0.39, 0.45, 0.58, and 0.65 e for He–Rn), as well as the trend in noble-gas atomic charge (Q^{VDD} = +0.26, +0.18, +0.42, +0.48, +0.54, and +0.58 a.u.; see Table 3). At this point, we stress that none of the methods for computing the amount of charge transfer yields absolute values; each of these approaches gains physical significance only through a comparison of trends in charge values, computed consistently with the same method along a series of species. For an extensive discussion of this issue, see reference [13a].

The trends that we compute here in the form of gross populations and VDD and Hirshfeld atomic charges are all consistent with increasing donor–acceptor orbital interaction and an increasing amount of electronic charge transfer from noble gas to methyl cation along He, Ne, Ar, Xe, Kr, and

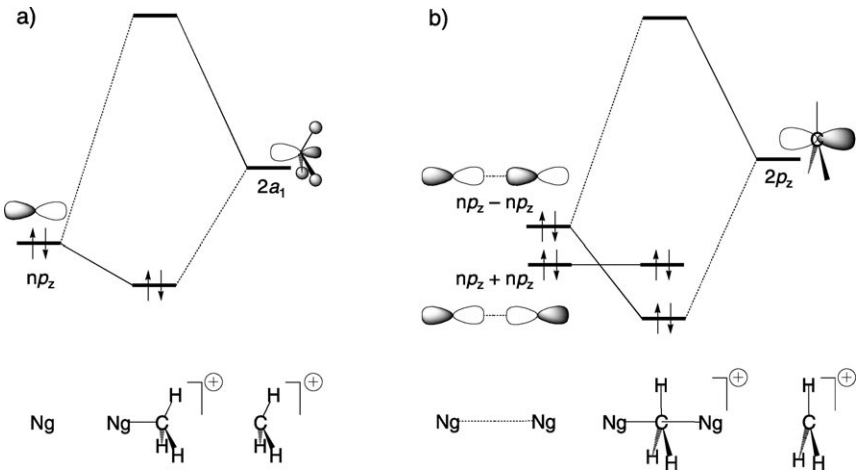

Figure 2. Generic frontier orbital interaction diagrams between Ng and CH_3^+ in CH_3Ng^+ (a) and between Ng···Ng and CH_3^+ in D_{3h}-symmetric $NgCH_3Ng^+$ (b), based on Kohn–Sham MO analyses at the (ZORA-)OLYP/TZ2P level. For Ng = He, the noble-gas AOs are 1s instead of np_z.

Rn. Note that whereas absolute values may differ significantly, each of the methods employed indicates that charge transfer is much smaller for the He and Ne complexes than for the heavier noble-gas complexes. In line with this, the extent of pyramidalization increases along this series, as reflected by the H-C-Ng angle θ (Table 3): 92.8 (He), 91.6 (Ne), 99.0 (Ar), 100.1 (Kr), 101.8 (Xe), and 102.3° (Rn). This can be understood in terms of the above-mentioned increase in the HOMO–LUMO interactions in ΔE_{oi} along this series, which works in two ways: 1) the HOMO–LUMO interaction itself directly ("electronically") induces pyramidalization because this deformation lowers the methyl $2a_1$ LUMO[15] and thus stabilizes the HOMO–LUMO interaction (see Figure 2a); 2) it also indirectly induces pyramidalization through approach of the (increasingly bulky) noble-gas atom, which sterically forces the substituents (i.e., the three hydrogen atoms) to bend backwards.[2d,e]

Importantly, however, the methyl moiety in the CH_3Ng^+ complexes is not that pyramidal at all. In fact, in CH_3He^+ and CH_3Ne^+ it is virtually planar, and the deviation from planarity for the heavier noble-gas complexes is only moderate, even in the most extreme case: CH_3Rn^+, in which θ is 102.3°. This is significantly less than in the isoelectronic methyl halides such as CH_3Cl, in which θ is 108.5°, close to the perfect tetrahedral angle of 109.5°. This can again be understood in terms of the longer and much weaker (heterolytic) C–Ng bond ($\Delta E = -2$ to -49 kcal mol^{-1}; see Table 3) as compared to the stronger (homolytic) C–X bond ($\Delta E = -86.5$ kcal mol^{-1} for CH_3Cl; not shown in Table 3; see also ref. [15]).

The preservation of a (nearly) planar, disk-shaped methyl unit in the CH_3Ng^+ species has led to the term "disk-and-ball" complex, used previously by Dopfer and coworkers.[4a,e] This notion also plays a central role in understanding the hypervalency (or "near hypervalency") of carbon in the $NgCH_3Ng^+$ systems, as will become clear below.

Structure and bonding in $[Ng{-}CH_3{-}Ng]^+$: The stabilization ΔE upon adding a second Ng atom to the backside of the methyl group in CH_3Ng^+ [see Eq. (5)] ranges from -0.6 (He) through -2.2 kcal mol^{-1} (Rn) and is thus even smaller than the already weak C–Ng bond strength associated with adding the first one to CH_3^+ [see Eq. (4)], as can be seen in Table 3 by comparing the ΔE values in parentheses [referring to Eq. (5)] to the corresponding values without parentheses [referring to Eq. (4)]. The approach of the second Ng atom slightly pushes the hydrogen atoms of the methyl moiety back towards the first Ng atom. Accordingly, the methyl fragment becomes about 1–2° less pyramidal, as measured by the H-C-Ng angle θ (compare θ values in Tables 3 and 4). Note that this is enough to make the methyl unit in $[He{-}CH_3{-}He]^+$ and $[Ne{-}CH_3{-}Ne]^+$ virtually planar, thus, yielding D_{3h}-symmetric equilibrium structures with a hypervalent carbon atom (see Table 4). The heavier noble-gas complexes, however, retain a C_{3v}-symmetric geometry $Ng{\cdots}CH_3Ng^+$ with a localized and a somewhat longer C–Ng bond.

Table 4. Analysis of C–Ng bonding between Ng···Ng and CH_3^+ in D_{3h} and C_{3v} stationary points of $NgCH_3Ng^+$ (Ng = He, Ne, Ar, Kr, Xe and Rn).[a]

	$HeCH_3He^+$[b]	$NeCH_3Ne^+$[b]	$ArCH_3Ar^+$[c]		$KrCH_3Kr^+$[c]		$XeCH_3Xe^+$[c]		$RnCH_3Rn^+$[c]	
	D_{3h}	D_{3h}	C_{3v}	D_{3h}	C_{3v}	D_{3h}	C_{3v}	D_{3h}	C_{3v}	D_{3h}
geometric parameters [Å, °]										
r_1(C–Ng)	2.123	2.395	2.030	2.429	2.153	2.539	2.281	2.697	2.372	2.775
r_2(C–Ng)	2.123	2.395	3.528	2.429	3.443	2.539	3.679	2.697	3.701	2.775
θ(H-C-Ng)	90.0	90.0	98.6	90.0	99.2	90.0	100.9	90.0	101.1	90.0
C–H	1.093	1.094	1.089	1.086	1.088	1.085	1.087	1.083	1.086	1.082
bond-energy decomposition [kcal mol^{-1}][d]										
ΔE_{oi}	−8.58	−10.60	−70.28	−48.66	−84.75	−63.65	−107.62	−81.14	−114.72	−90.92
ΔE_{Pauli}	7.57	7.37	54.56	34.49	58.84	41.04	67.74	47.38	66.30	49.58
ΔV_{elstat}	−1.36	−1.41	−11.73	−7.01	−12.23	−8.41	−13.66	−9.74	−12.39	−9.66
ΔE_{int}	−2.37	−4.64	−27.45	−21.17	−38.15	−31.02	−53.54	−43.49	−60.82	−50.99
ΔE_{prep}	0.01	0.01	5.54	0.08	6.35	0.11	8.98	0.17	9.27	0.25
ΔE	−2.36	−4.63	−21.91	−21.09	−31.80	−30.91	−44.56	−43.32	−51.55	−50.74
ΔE_{rel}[e]	(0.00)	0.00	0.00	0.82	(0.00)	(0.89)	0.00	1.24	0.00	0.81
$\langle Ng \mid CH_3^+ \rangle$ fragment orbital overlap										
⟨HOMO | LUMO⟩	0.215	0.135	0.220	0.247	0.243	0.267	0.256	0.283	0.258	0.285
⟨HOMO−1 | LUMO⟩	0.000	0.000	0.156	0.000	0.149	0.000	0.161	0.000	0.151	0.000
fragment orbital energy [eV]										
Ng···Ng: HOMO	−15.78	−13.60	−10.20	−10.18	−9.15	−9.13	−8.12	−8.09	−7.53	−7.50
Ng···Ng: HOMO−1	−15.79	−13.61	−10.22	−10.23	−9.18	−9.20	−8.16	−8.19	−7.58	−7.60
fragment orbital population [e]										
CH_3^+: LUMO	0.07	0.08	0.38	0.38	0.44	0.43	0.57	0.56	0.65	0.64
Noble-gas atomic charge [a.u.]										
Q^{VDD}	0.15	0.12	(0.23)[f]	0.23	(0.26)[f]	0.26	(0.29)[f]	0.30	(0.32)[f]	0.32
$Q^{Hirshfeld}$	0.09	0.11	(0.25)[f]	0.26	(0.30)[f]	0.31	(0.35)[f]	0.36	(0.37)[f]	0.39

[a] Computed at the OLYP/TZ2P level with ZORA relativistic effects for Ng = Kr, Xe, and Rn. See also Methods Section. [b] D_{3h}-symmetric $NgCH_3Ng^+$ structure is equilibrium geometry for Ng = He, Ne. [c] C_{3v} and D_{3h}-symmetric structures are equilibrium and S_N2 transition-state geometries, respectively, for Ng = Ar, Kr, Xe, Rn. [d] $\Delta E = \Delta E_{prep} + \Delta E_{int} = \Delta E_{prep} + \Delta V_{elstat} + \Delta E_{Pauli} + \Delta E_{oi}$. See also Methods Section. [e] $\Delta E_{rel} = \Delta E(D_{3h}) - \Delta E(C_{3v})$ = central barrier for S_N2 reaction of $Ng + CH_3Ng^+$. [f] Average of the atomic charges of each of the two Ng atoms.

In the following, we discuss the stability and bonding in $NgCH_3Ng^+$ species in terms of the energy ΔE associated with forming a complex from two noble-gas atoms and a methyl cation [Eq. (6)].

$$2\,Ng + CH_3^+ \rightarrow NgCH_3Ng^+ \quad (6)$$

The stability ΔE of equilibrium structures $NgCH_3Ng^+$, defined in this way, shows the same trend as that of CH_3Ng^+ [see Eq. (4)]: it increases monotonically on descending Group 18, from −2.4 (He) to −4.6 (Ne) to −21.9 (Ar) to −31.8 (Kr) to −44.6 (Xe) to −51.6 kcal mol^{-1} (Rn), as computed at the (ZORA-)OLYP/TZ2P level (see Table 4). As mentioned above, the $NgCH_3Ng^+$ species adopt D_{3h}-symmetric (hypervalent) structures for Ng = He and Ne. From Ng = Ar and down Group 18, the D_{3h}-symmetric species are S_N2 transition states that connect two equivalent C_{3v}-symmetric Ng···CH_3Ng^+ complexes via a relatively low central barrier of 0.8–1.2 kcal mol^{-1} (see ΔE_{rel} in Table 4).

The trend in ΔE derives again mainly from the systematic increase in the energy of the valence 1s or *n*p AOs along the series of noble-gas atoms, as follows from our analyses. Here we have analyzed ΔE in terms of the interaction ΔE_{int} between the Ng···Ng and CH_3^+ fragments plus the preparation energy ΔE_{prep} [see Eq. (2)]. This term consists of the energy change associated with bringing the two Ng atoms together in Ng···Ng, which is negligibly endothermic (i.e., 0.2 kcal mol^{-1} or less; not shown in Table 4), plus the energy change upon deforming the CH_3^+ fragment, which essentially makes up the entire preparation energy. Note, however, that ΔE_{prep} is somewhat smaller in $NgCH_3Ng^+$ (ΔE_{prep} = 0.01–9.27 kcal mol^{-1}) than in CH_3Ng^+ (0.19–11.38 kcal mol^{-1}) because the methyl group is less pyramidal in the former than in the latter (compare values in Tables 4 and 3, respectively). The trend in stability ΔE is determined by the trend in the actual interaction ΔE_{int} which, in turn, is dominated by the trend in the orbital interactions ΔE_{oi} (see Table 4).

This is very much like the situation for the C–Ng bond in CH_3Ng^+, discussed above, as is the fact that ΔE_{oi} stems to about 90% or more (values not shown in Table 4) from the donor–acceptor interactions between the occupied noble-gas valence AOs of Ng···Ng and the $2a_1$ LUMO of the methyl cation in the σ-electron system (values of ΔE_σ not shown in Table 4). In the Ng···Ng fragment, however, the noble gas AOs combine into bonding $np_z + np_z$ and antibonding $np_z - np_z$ fragment MOs, the HOMO−1 and HOMO of the σ-electron system (see Figure 2b). In the D_{3h}-symmetric structure, HOMO−1 has zero overlap with the $2a_1$ LUMO of the methyl cation (we adhere to using this C_{3v} symmetry label, for comparability with C_{3v}-symmetric Ng···CH_3Ng^+ and CH_3Ng^+ species). The donor–acceptor interaction is now provided only by the HOMO–LUMO interaction, which increases again as the orbital energy of the HOMO (−15.8 to 7.5 eV along the series) and the ⟨HOMO|LUMO⟩ overlap (0.14–0.29 along the series) increase on descending Group 18 (see Table 4). Note that the energies of the Ng···Ng HOMO and HOMO−1 both hardly differ from the noble gas AOs from which they are derived (compare orbital energies in Tables 4 and 3, respectively). This is because the noble-gas atoms in Ng···Ng have a relatively large separation of more than 4 Å and therefore experience only a very minor mutual interaction.

However, if the D_{3h}-symmetric species is allowed to relax towards bond-localized C_{3v}-symmetric equilibrium structure Ng···CH_3Ng^+ (Ng = Ar–Rn), the Ng···Ng HOMO−1 can also build up overlap with the CH_3^+ LUMO of about 0.15, while the ⟨HOMO|LUMO⟩ overlap is reduced by an amount of only 0.03 (see Table 4). This leads in all cases to net strengthening of the orbital interactions ΔE_{oi} and of the net interaction energy ΔE_{int}.

The question whether this extra stabilization upon C–Ng bond localization lowers the overall energy, and thus really happens, depends on whether the interaction is strong enough to surmount the deformation energy ΔE_{prep} needed to pyramidalize the rigid methyl cation. As can be seen in Table 4, the C–Ng interaction energy ΔE_{int} again shows (as in the case of the CH_3Ng^+ species) a strong increase from −4.6 to −21.2 kcal mol^{-1} if we go from D_{3h}-symmetric [Ne–CH_3–Ne]$^+$ to [Ar–CH_3–Ar]$^+$ and then further increases to −51.0 for [Rn–CH_3–Rn]$^+$. Going from D_{3h}-symmetric [Ar–CH_3–Ar]$^+$ to the C_{3v}-symmetric Ar···CH_3Ar^+, ΔE_{int} is stabilized by −6.3 kcal mol^{-1}, which is just enough to surmount the pyramidalization energy ΔE_{prep} of CH_3^+, which amounts to 5.5 kcal mol^{-1}. Note that even the total interaction energy ΔE_{int} of −2.4 and −4.6 kcal mol^{-1} in [He–CH_3–He]$^+$ and [Ne–CH_3–Ne]$^+$ is too small to surmount such a pyramidalization barrier (see Table 4). The methyl cation is too firmly bound and rigid to gain overall stabilization from C–Ng bond localization.

The methyl cation in [Ng–CH_3–Ng]$^+$ as a "disk between balls": The qualitative picture that emerges from our MO analyses is that CH_3^+ is a rigid, internally tightly bound "disk" with weaker contact to "balls" above and below, that is, the two noble-gas atoms. We designate this bonding situation "disk-between-balls" (DbB) model (see Scheme 2, top), in analogy to the term "disk-and-ball" complex used by Dopfer et al. for CH_3Ng^+ complexes.[4a,e] The resistance of the CH_3^+ fragment to pyramidalization is related to the strong and short C–H bonds, which cause the hydrogen atoms to be in close steric contact. Pyramidalization aggravates this steric repulsion and is therefore avoided.[15a]

However, the rigidity of the methyl moiety is a relative property: CH_3^+ is internally rigid compared to the weak carbon–axial substituent (C–X^{ax}) bond in the noble-gas complexes, especially for Ng = He and Ne. It is this situation that causes the breakdown of the ball-in-a-box (BiaB) model (Scheme 2, bottom). The latter explains why silicon in [Cl–SiH_3–Cl]$^-$ is hypervalent, whereas carbon in [Cl–CH_3–Cl]$^-$ is not. In terms of this model, silicon fits perfectly into the box that is constituted by the five substituents. Carbon, on the other hand, is too small and, in a sense, "drops to the bottom" of the box to give a species

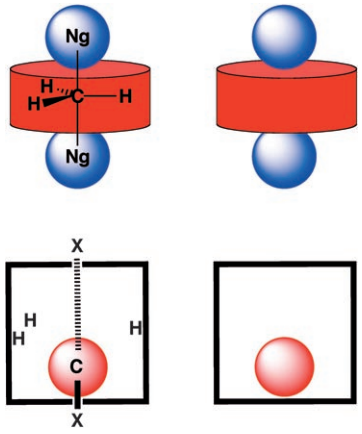

Scheme 2. Disk-between-balls (top) versus ball-in-a-box model (bottom) for five-coordinate carbon.

$Cl^-\cdots H_3CCl$ with one long C–Cl bond, one localized C–Cl contact, and a pyramidalized CH_3 unit. The validity of this model was shown to extend also to heavier Group 14 central atoms (Ge, Sn, Pb) and to another axial substituent (F). However, the BiaB picture is no longer a reasonable physical model if the carbon atom binds much more firmly to the "walls of the box" than to the "bottom", that is, if the carbon atom begins to form a much tighter subunit with the equatorial hydrogen atoms.

Thus, a switch occurs in the bonding capability of five-coordinate carbon from hypervalent (DbB model) to nonhypervalent (BiaB model) if the interaction with the axial substituents is strong enough that bond localization yields sufficient $C–X^{ax}$ bonding stabilization to compensate for the loss in stability in the methyl moiety that goes with the accompanying pyramidalization. Accordingly, all five-coordinate carbon species for which the BiaB model holds have much smaller differences between the strength of the carbon–equatorial hydrogen ($C–H^{eq}$) bond and the $C–X^{ax}$ bond: the former have weaker and the latter significantly stronger interaction energies. This can be nicely seen in Table 5, which lists the ΔE_{int} energies of $C–H^{eq}$ and $C–X^{ax}$ and their $C–H^{eq}/C–X^{ax}$ ratio for a series of isoelectronic, D_{3h}-symmetric $[X–CH_3–X]^q$ species that all share an X–C–X three-center, four-electron bonding motif. Thus, $[F–CH_3–F]^-$ and $[Cl–CH_3–Cl]^-$ have moderate $C–H^{eq}/C–X^{ax}$ ratios of 2.4–3.5, whereas the $C–H^{eq}/C–X^{ax}$ ratios of $[He–CH_3–He]^+$ and $[Ne–CH_3–Ne]^+$ are comparatively large (132 and 63, respectively).

Of course, the rigidity of the methyl moiety also depends on its effective valence configuration. Although all the species listed in Table 5 are isoelectronic, the $[Ng–CH_3–Ng]^+$ complexes effectively have a methyl-cation fragment, whereas the more conventional S_N2 transition states $[X–CH_3–X]^-$ effectively contain a methyl-radical fragment $CH_3^{\bullet}$, which resists pyramidalization much less than CH_3^+. This is illustrated in Figure 3, which shows the PES for pyramidalization of

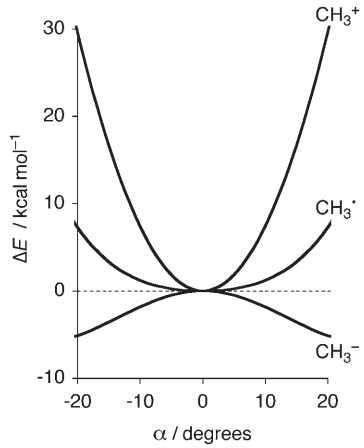

Figure 3. Relative energy of CH_3^+, $CH_3^{\bullet}$, and CH_3^- as a function of the pyramidalization angle $\alpha = \theta - 90°$ (see Scheme 1), computed at the OLYP/TZ2P level.

CH_3^+, $CH_3^{\bullet}$, and, for comparison, CH_3^-, which is even stabilized by adopting a pyramidal structure.[15a,16] At the same time, the C–H interaction energy also decreases in this order (see Table 5). Therefore, the somewhat simplifying criterion of the $C–H^{eq}/C–X^{ax}$ ratio of interaction energies is still valid, although it should not be overrated. On the other hand, this $C–H^{eq}/C–X^{ax}$ ratio criterion is in practice very straightforward to apply and therefore a powerful tool for categorizing five-coordinate carbon species as hypervalent (DbB) or nonhypervalent (BiaB).

Finally, we note that the data in Table 5 suggest a spectrum of bonding situations that runs from truly hypervalent (DbB model) to truly nonhy-

Table 5. Valency of the central carbon atom in terms of the spectrum of bonding situations between DbD and BiaB models.

Species	Bond strengths[a] $C–H^{eq}$	$C–X^{ax}$	Ratio	Model[b]	Barrier[c]	C valency
$[He–CH_3–He]^+$	−131.50	−1.00	131.5	DbB	0.0	hyper
$[Ne–CH_3–Ne]^+$	−130.89	−2.09	62.6	DbB	0.0	hyper
$[Ar–CH_3–Ar]^+$	−126.35	−6.25	20.2	DbB/BiaB	0.8	weakly nonhyper
$[Kr–CH_3–Kr]^+$	−124.49	−8.34	14.9	DbB/BiaB	0.9	weakly nonhyper
$[Xe–CH_3–Xe]^+$	−122.34	−10.47	11.7	DbB/BiaB	1.2	weakly nonhyper
$[Rn–CH_3–Rn]^+$	−121.22	−11.71	10.4	DbB/BiaB	0.8	weakly nonhyper
$[Cl–CH_3–Cl]^-$	−112.75	−31.88	3.5	BiaB	8.9	nonhyper
$[F–CH_3–F]^-$	−109.35	−44.65	2.4	BiaB	8.1	nonhyper

[a] Homolytic $C–H^{ax}$ and heterolytic $C–X^{eq}$ interaction energies ΔE_{int} [kcal mol^{-1}] between the corresponding molecular fragments frozen in the geometry they adopt in the overall D_{3h}-symmetric species; see also Methods Section and Equation (1). Computed at the OLYP/TZ2P level with ZORA relativistic effects for Ng = Kr, Xe, and Rn. [b] BiaB = ball in a box; DbB = disk between balls; DbB/BiaB = intermediate situation. [c] Central S_N2 barrier [kcal mol^{-1}].

pervalent (BiaB model) via a range of intermediate bonding situations (DbB/BiaB in Table 5). Of course, the transition from hypervalent (stable D_{3h}-symmetric species) to nonhypervalent (labile D_{3h}-symmetric species) cannot be taken as a sharp border between DbB and BiaB, and the choice of where to classify the situation as intermediate or "weakly nonhypervalent" is certainly associated with some arbitrariness. Yet, it is also a fact that the propensity of the system to localize one of its C–X^{ax} bonds and to expand the other smoothly increases on going down Table 5. We feel that it is possible to conceive of the $[Ng–CH_3–Ng]^+$ complexes with intermediate C–H^{eq}/C–X^{ax} ratios (ca. 10–20 for Ng = Rn, Xe, Kr, Ar) as distorted DbB complexes as well as species that show BiaB behavior. Here, in Table 5, we have chosen to classify the species with S_N2 central barriers of about 0, 1, and 10 kcal mol^{-1} as truly hypervalent (DbB), "weakly hypervalent (DbB/BiaB), and truly nonhypervalent (BiaB), respectively.

Comparison with $[Ng–H]^+$ and $[Ng–H–Ng]^+$: Finally, we compare the disk-and-ball and disk-between-balls complexes CH_3Ng^+ and $NgCH_3Ng^+$, respectively, with the corresponding protonated noble-gas atoms and proton-bound noble-gas dimers. The above results show that, if the central $[CH_3]$ unit is sufficiently tightly bound and rigid, then stable, hypervalent $[X–CH_3–X]^q$ structures occur. This also nicely agrees with the finding of a previous study that $[Cl–C–Cl]^{-‴}$, which is isoelectronic to the labile transition state $[Cl–CH_3–Cl]^-$, also forms a stable symmetric structure with two equivalent C–Cl bonds.[1]

Indeed, the proton-bound noble-gas dimers adopt $D_{\infty h}$-symmetric, hypervalent [Ng-H-Ng]$^+$ equilibrium structures with Ng–H distances that monotonically increase from 0.939 (He) to 1.169 (Ne) to 1.533 (Ar) to 1.685 (Kr) to 1.890 (Xe) to 1.986 Å (Kr), as can be seen in Table 6. The stabilization ΔE associated with complexation of the proton with the first noble-gas atom [Eq. (7)] increases monotonically from −46.7 (He) to −52.8 (Ne) to −96.6 (Ar) to −109.0 (Kr) to −125.4 (Xe) to −133.9 kcal mol^{-1} (Rn), in good agreement with previous computations of the proton affinities (PA = $-\Delta E$) of these species at the ZORA-BP86/TZ2P level.[17]

$$Ng + H^+ \rightarrow NgH^+ \quad (7)$$

The stabilization ΔE associated with the complexation of NgH^+ with the second noble-gas atom [see Eq. (8)] is consistently smaller but also increases (although not entirely monotonically) from −14.7 kcal mol^{-1} for $HeHHe^+$ to −18.2 kcal mol^{-1} for $RnHRn^+$ (see Table 6).

$$NgH^+ + Ng \rightarrow NgHNg^+ \quad (8)$$

This resembles the situation described above for the corresponding methyl-cation complex, for which complexation with the first noble-gas atom Ng also yields a larger stabilization than complexation of CH_3Ng^+ with a second Ng (see Table 3). Also, the bonding mechanism of the proton complexes is very similar to that of the methyl-cation complexes. It arises from a strong HOMO–LUMO interaction between the occupied noble gas 1s (He) or *n*p (Ne–Rn) valence AOs with the unoccupied proton 1s acceptor orbital. This is associated with a sizeable charge transfer, as reflected by the large positive charge of the noble-gas atoms Q^{VDD}, which ranges from +0.44 a.u. in HeH^+ to +0.70 a.u. in RnH^+ (see Table 6).

There is, however, also a marked difference between the methyl-cation and proton complexes. The bond energies in CH_3Ng^+ (−1.7 to −49.3 kcal mol^{-1}, see Table 3) are much lower than in the corresponding NgH^+ (−46.7 to −133.9 kcal mol^{-1}, see Table 6). The main reason for this large difference in bond energies is the Pauli repulsion ΔE_{Pauli} with closed-shell orbitals in CH_3^+ and the complete absence of such repulsion with H^+, which has no closed shells (compare Table 4 and Table 6, respectively). The only force that prevents the Ng–H bond length collapsing to zero is the nuclear–nuclear repulsion. Thus, whereas the electrostatic interaction ΔV_{elstat} is in general attractive,[7a] all NgH^+

Table 6. Analysis of Ng–H bonding between Ng and H^+ in NgH^+ and between Ng···Ng and H^+ in $NgHNg^+$ (Ng = He, Ne, Ar, Kr, Xe and Rn).[a]

	HeH^+	He_2H^+	NeH^+	Ne_2H^+	ArH^+	Ar_2H^+	KrH^+	Kr_2H^+	XeH^+	XeH^+	RnH^+	Rn_2H^+
r(Ng–H) [Å]	0.789	0.939	1.014	1.169	1.297	1.533	1.433	1.685	1.612	1.890	1.702	1.986
bond-energy decomposition [kcal mol^{-1}][b]												
ΔE_{oi}	−75.94	−93.90	−79.63	−98.82	−134.91	−148.23	−147.84	−161.76	−164.18	−176.56	−171.72	−186.50
ΔE_{Pauli}	0.00	0.00	0.00	0.00	0.00	0.00	0.00	0.00	0.00	0.00	0.00	0.00
ΔV_{elstat}	29.24	29.64	26.83	26.36	38.31	30.29	38.82	30.72	38.82	29.75	37.84	30.58
ΔE_{int}	−46.69	−64.26	−52.80	−72.46	−96.60	−117.94	−109.02	−131.04	−125.36	−146.81	−133.88	−155.92
ΔE_{prep}	0.00	2.85	0.00	2.43	0.00	3.88	0.00	3.99	0.00	3.94	0.00	3.81
ΔE	−46.69	−61.41	−52.80	−70.03	−96.60	−114.06	−109.02	−127.05	−125.36	−142.87	−133.88	−152.11
ΔE[c]		−14.71		−17.22		−17.46		−18.03		−17.51		−18.22
noble-gas atomic charge [a.u.]												
Q^{VDD}	0.44	0.32	0.44	0.31	0.57	0.37	0.63	0.40	0.66	0.42	0.70	0.43
$Q^{Hirshfeld}$	0.41	0.30	0.49	0.35	0.66	0.42	0.72	0.44	0.78	0.47	0.82	0.48

[a] Computed at the OLYP/TZ2P level with ZORA relativistic effects for Ng = Kr, Xe, and Rn. See also Methods Section. NgH^+ and $NgHNg^+$ species are $C_{\infty v}$- and $D_{\infty h}$-symmetric equilibrium structures, respectively. [b] $\Delta E = \Delta E_{prep} + \Delta E_{int} = \Delta E_{prep} + \Delta V_{elstat} + \Delta E_{Pauli} + \Delta E_{oi}$. For $NgHNg^+$ species ($n = 2$), ΔE_{prep} is the energy associated with combining two separate Ng atoms into the Ng···Ng fragment; see also Methods Section. [c] For comparison: ΔE associated with adding a second Ng to HNg^+ with formation of the $NgHNg^+$ equilibrium structure.

species show pronouncedly positive (i.e., destabilizing) values between roughly 27 and 38 kcal mol^{-1} (see Table 6).

Conclusion

The ball-in-a-box model that we recently introduced explains why silicon in $[Cl{-}SiH_3{-}Cl]^-$ is hypervalent whereas carbon in $[Cl{-}CH_3{-}Cl]^-$ is not. In terms of this model, silicon fits perfectly into the box that is constituted by the five substituents. Carbon, on the other hand, is too small and, in a sense, "drops to the bottom" of the box to give a species $Cl^-\cdots H_3CCl$ with one long C–Cl bond, one localized C–Cl contact, and a pyramidalized CH_3 unit. The validity of this model was shown to extend also to heavier Group 14 central atoms (Ge, Sn, Pb) and another axial substituent (F).

In the present study, however, we encountered species that violate this ball-in-a-box behavior: although isostructural and isoelectronic with the above $[X{-}CH_3{-}X]^-$ systems, the noble gas/methyl cation complexes $[Ng{-}CH_3{-}Ng]^+$ adopt, for Ng = helium and neon, a perfectly D_{3h}-symmetric structure featuring a stable hypervalent carbon atom with two equivalent C–Ng bonds. Our analyses show that the carbon atom in $[Ng{-}CH_3{-}Ng]^+$ can no longer be considered as a ball in a box of the five substituents, because it is much more tightly bound to the equatorial H atoms than to the axial noble-gas substituents. Thus, the $[Ng{-}CH_3{-}Ng]^+$ species are better conceived as a "disk between balls". Here, the "disk" is CH_3^+ and the "balls" are the two noble-gas atoms.

Finally, we propose to classify the nature of five-coordinate carbon species in terms of a spectrum between the ball-in-a-box situation (nonhypervalent C) and the disk-between-balls model (hypervalent C). The position along this spectrum is determined by the ratio (i.e., the relative magnitudes) of the strengths of the carbon–equatorial substituent bond ($C{-}H^{eq}$) and the carbon–axial substituent bond ($C{-}X^{ax}$). Hypervalent species have large $C{-}H^{eq}/C{-}X^{ax}$ ratios (here: 63–132), whereas truly nonhypervalent species have small $C{-}H^{eq}/C{-}X^{ax}$ ratios (here: 2.4–3.5). Intermediate or "weakly nonhypervalent" cases (i.e., species with a weak tendency to localize one and to partly break the other axial carbon–substituent bond), such as $[Ng{-}CH_3{-}Ng]^+$ complexes with heavy noble-gas atoms, have intermediate $C{-}H^{eq}/C{-}X^{ax}$ ratios (here: 10–20).

Acknowledgements

We thank the Netherlands Organization of Scientific Research (NWO-CW) for financial support. A Marie Curie fellowship for J.P. is gratefully acknowledged. We also thank the Departament d'Universitats, Recerca i Societat de la Informació (DURSI) of the Generalitat de Catalunya for the postdoctoral fellowship 2004BE00028 for J.P.

[1] a) S. C. A. H. Pierrefixe, C. Fonseca Guerra, F. M. Bickelhaupt, *Chem. Eur. J.* **2008**, *14*, 819.

[2] Examples of related work: a) R. Hoffmann, J. M. Howell, E. L. Muetterties, *J. Am. Chem. Soc.* **1972**, *94*, 3047; b) G. C. Pimentel, *J. Chem. Phys.* **1951**, *19*, 446; c) R. J. Hach, R. E. Rundle, *J. Am. Chem. Soc.* **1951**, *73*, 4321; d) A. P. Bento, F. M. Bickelhaupt, *J. Org. Chem.* **2007**, *72*, 2201; e) M. A. van Bochove, M. Swart, F. M. Bickelhaupt, *J. Am. Chem. Soc.* **2006**, *128*, 10738.

[3] a) M. B. Smith, J. March, *March's Advanced Organic Chemistry*, 6th ed., Wiley-Interscience, New York, **2007**; b) S. S. Shaik, H. B. Schlegel, S. Wolfe, *Theoretical Aspects of Physical Organic Chemistry: The S_N2 Mechanism*, Wiley, New York, **1992**; c) J. K. Laerdhal, E. Uggerud, *Int. J. Mass Spectrom.* **2002**, *214*, 277.

[4] a) E. J. Bieske, O. Dopfer, *Chem. Rev.* **2000**, *100*, 3963, and references therein; b) K. Hiraoka, I. Kudaka, S. Yamabe, *Chem. Phys. Lett.* **1991**, *178*, 103; c) R. V. Olkhov, S. A. Kizkorodov, O. Dopfer, *J. Chem. Phys.* **1998**, *108*, 10046; d) R. V. Olkhov, S. A. Kizkorodov, O. Dopfer, *J. Chem. Phys.* **1999**, *110*, 9527; e) O. Dopfer, R. V. Olkhov, J. P. Maier, *J. Chem. Phys.* **2000**, *112*, 2176; f) R. W. Gora, S. Roszak, J. Leszczynski, *J. Chem. Phys.* **2001**, *115*, 771; g) O. Dopfer, D. Luckhaus, *J. Chem. Phys.* **2002**, *116*, 1012; h) O. Dopfer, *Int. Rev. Phys. Chem.* **2003**, *22*, 437; i) A. Cunje, A. C. Hopkinson, S. Yamabe, K. Hiraoka, F. Nakagawa, M. Ishida, K. Fujita, K. Takao, A. Wada, K. Hiizumi, *J. Phys. Chem. A* **2004**, *108*, 11218.

[5] a) G. te Velde, F. M. Bickelhaupt, E. J. Baerends, C. Fonseca Guerra, S. J. A. van Gisbergen, J. G. Snijders, T. Ziegler, *J. Comput. Chem.* **2001**, *22*, 931; b) C. Fonseca Guerra, J. G. Snijders, G. te Velde, E. J. Baerends, *Theor. Chem. Acc.* **1998**, *99*, 391; c) E. van Lenthe, E. J. Baerends, J. G. Snijders, *J. Chem. Phys.* **1994**, *101*, 9783; d) E. J. Baerends, J. Autschbach, A. Bérces, J. A. Berger, F. M. Bickelhaupt, C. Bo, P. L. de Boeij, P. M. Boerrigter, L. Cavallo, D. P. Chong, L. Deng, R. M. Dickson, D. E. Ellis, M. van Faassen, L. Fan, T. H. Fischer, C. Fonseca Guerra, S. J. A. van Gisbergen, J. A. Groeneveld, O. V. Gritsenko, M. Grüning, F. E. Harris, P. van den Hoek, C. R. Jacob, H. Jacobsen, L. Jensen, E. S. Kadantsev, G. van Kessel, R. Klooster, F. Kootstra, E. van Lenthe, D. A. McCormack, A. Michalak, J. Neugebauer, V. P. Nicu, V. P. Osinga, S. Patchkovskii, P. H. T. Philipsen, D. Post, C. C. Pye, W. Ravenek, P. Romaniello, P. Ros, P. R. T. Schipper, G. Schreckenbach, J. G. Snijders, M. Solà, M. Swart, D. Swerhone, G. te Velde, P. Vernooijs, L. Versluis, L. Visscher, O. Visser, F. Wang, T. A. Wesolowski, E. M. van Wezenbeek, G. Wiesenekker, S. K. Wolff, T. K. Woo, A. L. Yakovlev, T. Ziegler, ADF2007, ##Scientific Computing & Modeling, Amsterdam, The Netherlands, **2007**.

[6] a) C. Lee, W. Yang, R. G. Parr, *Phys. Rev. B* **1988**, *37*, 785; b) N. C. Handy, A. Cohen, *Mol. Phys.* **2001**, *99*, 403; c) A. D. Becke, *Phys. Rev. A* **1988**, *38*, 3098; d) J. P. Perdew, *Phys. Rev. B* **1986**, *33*, 8822; Erratum: *Phys. Rev. B* **1986**, *34*, 7406.

[7] a) F. M. Bickelhaupt, E. J. Baerends, in *Reviews in Computational Chemistry, Vol. 15* (Eds.: K. B. Lipkowitz, D. B. Boyd), Wiley, New York, **2000**, p. 1–86; b) F. M. Bickelhaupt, N. M. M. Nibbering, E. M. van Wezenbeek, E. J. Baerends, *J. Phys. Chem.* **1992**, *96*, 4864; c) T. Ziegler, A. Rauk, *Inorg. Chem.* **1979**, *18*, 1755; d) T. Ziegler, A. Rauk, *Inorg. Chem.* **1979**, *18*, 1558; e) T. Ziegler, A. Rauk, *Theor. Chim. Acta* **1977**, *46*, 1.

[8] a) C. Møller, M. S. Plesset, *Phys. Rev.* **1934**, *46*, 618; b) J. J. Cizek, *Chem. Phys.* **1966**, *45*, 4256; c) K. Raghavachari, G. W. Trucks, J. A. Pople , M. Headgordon, *Chem. Phys. Lett.* **1989**, *157*, 479.

[9] Gaussian 03, Revision B.02, M. J. Frisch, G. W. Trucks, H. B. Schlegel, G. E. Scuseria, M. A. Robb, J. R. Cheeseman, J. A. Montgomery, Jr., T. Vreven, K. N. Kudin, J. C. Burant, J. M. Millam, S. S. Iyengar, J. Tomasi, V. Barone, B. Mennucci, M. Cossi, G. Scalmani, N. Rega, G. A. Petersson, H. Nakatsuji, M. Hada, M. Ehara, K. Toyota, R. Fukuda, J. Hasegawa, M. Ishida, T. Nakajima, Y. Honda, O. Kitao, H. Nakai, M. Klene, X. Li, J. E. Knox, H. P. Hratchian, J. B. Cross, C. Adamo, J. Jaramillo, R. Gomperts, R. E. Stratmann, O. Yazyev, A. J. Austin, R. Cammi, C. Pomelli, J. W. Ochterski, P. Y. Ayala, K. Morokuma, G. A. Voth, P. Salvador, J. J. Dannenberg, V. G. Zakrzewski, S. Dapprich, A. D. Daniels, M. C. Strain, O. Farkas, D. K. Malick, A. D. Rabuck, K. Raghavachari, J. B. Foresman, J. V. Ortiz, Q. Cui, A. G. Baboul, S. Clifford, J. Cioslowski,

B. B. Stefanov, G. Liu, A. Liashenko, P. Piskorz, I. Komaromi, R. L. Martin, D. J. Fox, T. Keith, M. A. Al-Laham, C. Y. Peng, A. Nanayakkara, M. Challacombe, P. M. W. Gill, B. Johnson, W. Chen, M. W. Wong, C. Gonzalez, J. A. Pople, Gaussian, Inc., Pittsburgh, PA, **2003**.
[10] M. J. Frisch, J. A. Pople, J. S. Binkley, *J. Chem. Phys.* **1984**, *80*, 3265.
[11] T. H. Dunning Jr. , *J. Chem. Phys.* **1989**, *90*, 1007.
[12] K. Morokuma, *Acc. Chem. Res.* **1977**, *10*, 294.
[13] a) C. Fonseca Guerra, J.-W. Handgraaf, E. J. Baerends, F. M. Bickelhaupt, *J. Comput. Chem.* **2004**, *25*, 189; b) F. M. Bickelhaupt, N. J. R. van Eikema Hommes, C. Fonseca Guerra, E. J. Baerends, *Organometallics* **1996**, *15*, 2923; c) C. Fonseca Guerra, F. M. Bickelhaupt, J. G. Snijders, E. J. Baerends, *Chem. Eur. J.* **1999**, *5*, 3581.
[14] F. L. Hirshfeld, *Theor. Chim. Acta* **1977**, *44*, 129.
[15] a) F. M. Bickelhaupt, T. Ziegler, P. v. R. Schleyer, *Organometallics* **1996**, *15*, 1477; b) L. Deng, V. Branchadell, T. Ziegler, *J. Am. Chem. Soc.* **1994**, *116*, 10645.
[16] T. A. Albright, J. K. Burdett, M.-H. Whangbo, *Orbital Interactions in Chemistry*, Wiley, New York, **1985**.
[17] M. Swart, E. Rösler, F. M. Bickelhaupt, *J. Comput. Chem.* **2006**, *27*, 1486.

Received: January 4, 2008
Published online: June 24, 2008

